Monitoring-Induced Seismicity in Urban Environment Using Low-Cost Stations: Lessons Learned from the Strasbourg Dense Semipermanent Seismic Network, France

Riccardo Minetto*[1], Olivier Lengliné[1], Mathieu Turlure[1], Marc Grunberg[1], Sophie Lambotte[1], Antoine Schlupp[1], Jérôme Vergne[2], Benoit Derode[1], and Jean Schmittbuhl[1]

Abstract

With the growing number of geothermal energy projects near urban centers, monitoring seismicity in urban environments is becoming increasingly important. In recent years, the introduction of low-cost stations such as Raspberry Shake stations has provided a viable means of densifying seismic networks and enabling long-term monitoring in cities. However, their effectiveness compared to traditional stations remains to be assessed. In this study, we focus on the dense semipermanent seismic network (DSSN), which is primarily composed of Raspberry Shake stations and was deployed to monitor seismicity at the Vendenheim deep geothermal site near Strasbourg, France. Specifically, using the recorded noise at the stations, we evaluate the network's ability to detect and locate local earthquakes. Our results show that detection and location performance vary significantly between day and night. These limitations can be mitigated either by complementing the DSSN with stations installed in quieter environments outside the urban area or by densifying the DSSN itself, up to a critical station density corresponding to a minimum interstation distance of about 2 km. In addition, we find that Raspberry Shake stations installed in private homes experience noise levels comparable to those of broadband stations located in public or commercial buildings. Our study shows that low-cost stations can contribute to high-resolution earthquake catalogs in urban environments alongside traditional stations. However, achieving consistent detection and location levels throughout the day can require high station density, careful site selection, and the inclusion of stations less affected by anthropogenic noise.

Cite this article as Minetto, R., O. Lengliné, M. Turlure, M. Grunberg, S. Lambotte, A. Schlupp, J. Vergne, B. Derode, and J. Schmittbuhl (2025). Monitoring-Induced Seismicity in Urban Environment Using Low-Cost Stations: Lessons Learned from the Strasbourg Dense Semipermanent Seismic Network, France, *Seismol. Res. Lett.* **XX**, 1–14, doi: 10.1785/0220250248.

Supplemental Material

Introduction

Fluids extracted from deep geothermal reservoirs provide a means to harness the Earth's internal heat. High-temperature geothermal fluids can be used to generate electricity, but they are more efficiently used for direct heating applications, such as urban heating networks and industrial processes (Horne *et al.*, 2025). Unlike electricity, heat cannot be efficiently transported over long distances, so fluid extraction and reinjection typically take place near the urban and industrial centers that benefit from the extracted heat.

The extraction and reinjection operations involved in geothermal energy production can alter subsurface stress conditions, causing anthropogenic (induced) seismic activity (e.g., Moein *et al.*, 2023). Although these earthquakes are typically small ($M < 3$), past experiences have shown that geothermal operations can induce earthquakes large enough to be felt by the population, damage buildings, and consequently lead to the complete cessation of well activities (Batterman *et al.*,

1. EOST/ITES, Strasbourg University/CNRS, Strasbourg, France, https://orcid.org/0000-0002-6797-5190 (RM); https://orcid.org/0000-0003-0678-2587 (OL); https://orcid.org/0009-0005-3175-7000 (MT); https://orcid.org/0000-0002-1307-7790 (MG); https://orcid.org/0000-0003-1078-3419 (SL); https://orcid.org/0000-0003-2375-1782 (BD); https://orcid.org/0000-0002-7000-0618 (JS); 2. Institut de physique du globe de Paris (IPGP), Université Paris Cité, CNRS, Paris, France, https://orcid.org/0000-0003-1731-9360 (JV)

*Corresponding author: minetto.riccardo@gmail.com

2021; Schmittbuhl *et al.*, 2021). Therefore, it is essential to have a dedicated seismic network to monitor seismicity and improve seismic hazard assessment (Zhou *et al.*, 2024). Ideally, this network should record continuously not only during injection, but also before and after injection to assess background seismicity and capture trailing seismicity (Herrmann *et al.*, 2019; Lengliné *et al.*, 2023). The network should also have sufficient station coverage to accurately estimate earthquake source parameters and to detect enough earthquakes to perform statistical analyses.

However, monitoring seismicity in urban environments presents several challenges. High-noise levels, especially during the day, limit earthquake detection. In addition, finding suitable installation sites can be logistically challenging due to factors such as property access rights or interference from urban infrastructure. These limitations do not only affect earthquake monitoring, but also other applications of urban networks (Scudero *et al.*, 2023) such as earthquake early warning (Zülfikar *et al.*, 2017; Henao Casas and Monsalve, 2018; Patanè *et al.*, 2022; Vitale *et al.*, 2022), postevent damage assessment (Costanzo *et al.*, 2021; Miura *et al.*, 2023), seismic intensity mapping (Clayton *et al.*, 2015), site effect research (Layadi *et al.*, 2016; Frankel and Grant, 2020; Pacheco *et al.*, 2022; Janusz *et al.*, 2024), and structural health monitoring (Çelebi, 2019; Clayton *et al.*, 2019).

One way to overcome these limitations is to record seismicity using stations that are far away from the injection point but located in an environment protected from anthropogenic noise. The main drawback of this approach is that distant stations offer a limited contribution in constraining earthquake location, especially in depth. Therefore, despite the adverse conditions, it remains essential to record the seismicity using stations deployed within the urban area.

Several types of networks can be used to record seismicity within an urban area, each with its own advantages and limitations. Borehole stations provide high-quality recordings because the level of anthropogenic noise is significantly reduced at depth. However, the high cost of drilling and borehole stations typically restricts their number, leading to networks with potentially good temporal coverage but limited spatial coverage (Bethmann *et al.*, 2012; Vasterling *et al.*, 2017; Küperkoch *et al.*, 2018). Seismic arrays, composed of a large number of closely spaced stations, offer high spatial coverage, which can help mitigate the high noise levels typically found in urban environments (Li *et al.*, 2018; Lythgoe *et al.*, 2021; Fiori *et al.*, 2023). However, their high deployment cost generally limits their use to short periods of time (days to a few months). Seismicity can also be monitored using a dedicated surface network, typically composed of broadband, short-period, or accelerometric stations (Bethmann *et al.*, 2012; Hillers *et al.*, 2020). These networks can provide good long-term coverage, but the relatively high cost of the sensors and the logistical challenges of finding suitable long-term installation sites may limit the number of stations and thus the spatial coverage of the network, though to a lesser extent than borehole station networks.

In recent years, low-cost stations, such as Raspberry Shake stations (Anthony *et al.*, 2018), have emerged as a viable alternative to traditional stations in urban areas. These stations offer the advantage of easy deployment in buildings and low maintenance costs, although their natural frequency (0.5 Hz) is higher than that of broadband stations (about 0.01 Hz). Because of these features, Raspberry Shake stations have been successfully used to complement existing urban networks (Calais *et al.*, 2019; Holmgren and Werner, 2021; Hughes *et al.*, 2025) and promote collaboration between citizens and scientists (Diaz *et al.*, 2020; Subedi *et al.*, 2020; Schlupp *et al.*, 2023), which could be crucial in mitigating the social impact of these projects.

An example of an urban Raspberry Shake network is the dense semipermanent seismic network (DSSN) of the Strasbourg Eurométropole. This network has several unique features: (1) Since 2022, stations have been installed in the homes of volunteer citizens as part of a participatory science project, which has been ongoing ever since. (2) Stations are seamlessly integrated into the Bureau Central Sismologique Français and Réseau National de Surveillance Sismique (BCSF-Rénass) network. (3) Thanks to the installation of the first stations in 2017, the network was able to monitor seismic activity before and during injection operations at the Vendenheim (Geoven) geothermal site. These operations began in 2018 and ceased in early 2021 after an M_L 3.3 event, with the largest earthquake (M_L 3.9) occurring approximately six months after injection ended (Lengliné *et al.*, 2023). (4) As of December 2024, the network comprises 38 active stations deployed across an area of 17 × 27 km, with a significant percentage of these stations being Raspberry Shake stations. For details on the installation and the volunteer recruitment process, we refer to Text S1, available in the supplemental material to this article.

In this study, we used the Strasbourg Eurométropole DSSN stations to explore the possible advantages and limitations of recording seismicity in urban areas using low-cost sensors. In particular, our objectives are to

- compare the detection performance of Raspberry Shake stations and permanent stations installed in an urban environment;
- evaluate the benefits of recording seismicity in a heavily urbanized area, or, in other words, if stations closer to the expected epicenters but in a noisy environment can offer better detection performance than stations farther from the epicenter but installed in a less noisy environment; and
- determine how increasing the number of stations affects the detection and location performance of the network under different noise conditions.

To assess the detection and location performance of the DSSN, we examine how the detection levels and location

uncertainties of modeled earthquakes for which source properties are calibrated using the source properties of the events recorded during the Vendenheim sequence vary in response to diurnal fluctuations in the noise levels recorded at the DSSN stations.

Data

We refer to the Strasbourg DSSN as the network comprising all seismic stations located within the Strasbourg Eurométropole and active after January 2018. This includes both Raspberry Shake and broadband stations.

In this study, we selected all Strasbourg DSSN stations active between January 2018 and December 2024, excluding those with less than three months of data or known to be defective. This resulted in a total of 49 stations (Fig. 1 and Fig. S1). Among them, eight are three-component broadband stations recording at 200 Hz belonging to the Epos-France permanent network (four stations) and to a temporary network installed to monitor induced seismicity at the Vendenheim deep geothermal site (four stations). The remaining 41 stations are Raspberry Shake stations, recording either only the vertical component at 50 Hz (six stations) or all three components at 100 Hz (35 stations). Approximately half of the Raspberry Shake stations were installed after September 2023, whereas the rest were mostly deployed in mid-2017 and late 2020. We point out that their installation was preceded by calibration tests to ensure that the instrument response of the sensors is consistent with that provided by the manufacturer. These tests revealed that the amplitude spectra closely follow the expected response. However, phase spectra show deviations above 2 Hz at most stations, which become significant above 10 Hz (Fig. S1). Additional details about the calibration tests are provided in the supplemental material (Text S1).

In our analysis, we also included 11 permanent stations located outside the Strasbourg Eurométropole and within a 45 km radius of the Vendenheim injection site (Fig. 1). This is the radius needed to include all stations that were used to detect and locate more than one event of the Vendenheim sequence found in the BCSF-Rénass catalog. This selection criterion was chosen to conservatively exclude stations that are either too far from the study area or strongly affected by noise to contribute to the analysis. These stations are three-component broadband or short-period stations recording at either 100 or 200 Hz. Among them, nine belong to the EPOS-France permanent network and two to the Erdbebendienst Südwest network.

2018–2022 Vendenheim seismic sequences

Between 2018 and 2021, fluids were injected through two wells during the course of several stages (Schmittbuhl *et al.*, 2021). The injection of fluids was accompanied by seismic activity that reached M_L 3.9 in July 2021, six months after the shut-in of the wells and after an event M_L 3.6 (Lengliné *et al.*, 2023). In this study, we used the events of the Vendenheim sequence, part of the BCSF-Rénass catalog. This catalog consists of 582 events that occurred between March 2018 and November 2022.

Methods

A common way to evaluate network performance is to study the spatiotemporal variability of the magnitude of completeness (M_c). The selection of a suitable method to derive M_c is strictly dependent on the spatiotemporal distribution of earthquakes that occur within the network. In the case of the Vendenheim sequence, earthquakes are clustered both in space and time (Fig. S2). This prevents the use of methods only based on observed earthquakes (e.g., Schorlemmer and Woessner, 2008; Mignan *et al.*, 2011), as a large number of events spread over space are typically needed to obtain robust relationships between M_c and distance. To overcome this limitation, we used the wideband spectral ratio (WSR) method (Schultz *et al.*, 2015). This method only requires the noise information observed at the stations and the theoretical spectra of earthquakes located within the area of interest. Its advantage is that the number, position, and size of earthquakes can be freely chosen. In addition, the properties of the theoretical spectra can be calibrated using the information derived from the observed seismicity and the geology of the area.

Estimation of M_c with the WSR method

The WSR is defined as

$$\mathrm{WSR} = \frac{\sqrt{P_S}}{\sqrt{P_N}}, \tag{1}$$

in which P_N is the noise power and P_S is the signal power. At a given station, P_N is defined as the integral of the modal noise power spectral density (PSD) N_m, which is derived from the probabilistic PSD (PPSD) calculated over a specified time period (McNamara and Buland, 2004),

$$P_N = \frac{1}{f_2 - f_1}\int_{f_1}^{f_2} N_m \mathrm{d}f, \tag{2}$$

in which f_1 and f_2 are the lower and upper frequencies that define the integration interval, respectively. Using the modal PSD ensures that the P_N estimate reflects the most common noise conditions, typically dominated by working-day activity, and thus minimizes the influence of atypical events such as the COVID-19 pandemic (Lecocq *et al.*, 2020).

For a given earthquake, P_S is estimated from its theoretical PSD $|\tilde{S}|^2$,

$$P_S = \frac{1}{f_2 - f_1}\int_{f_1}^{f_2} |\tilde{S}|^2 \mathrm{d}f, \tag{3}$$

in which $\tilde{S}$ is the theoretical amplitude spectrum derived from the Brune source model (Brune, 1970). We refer to Text S2 for

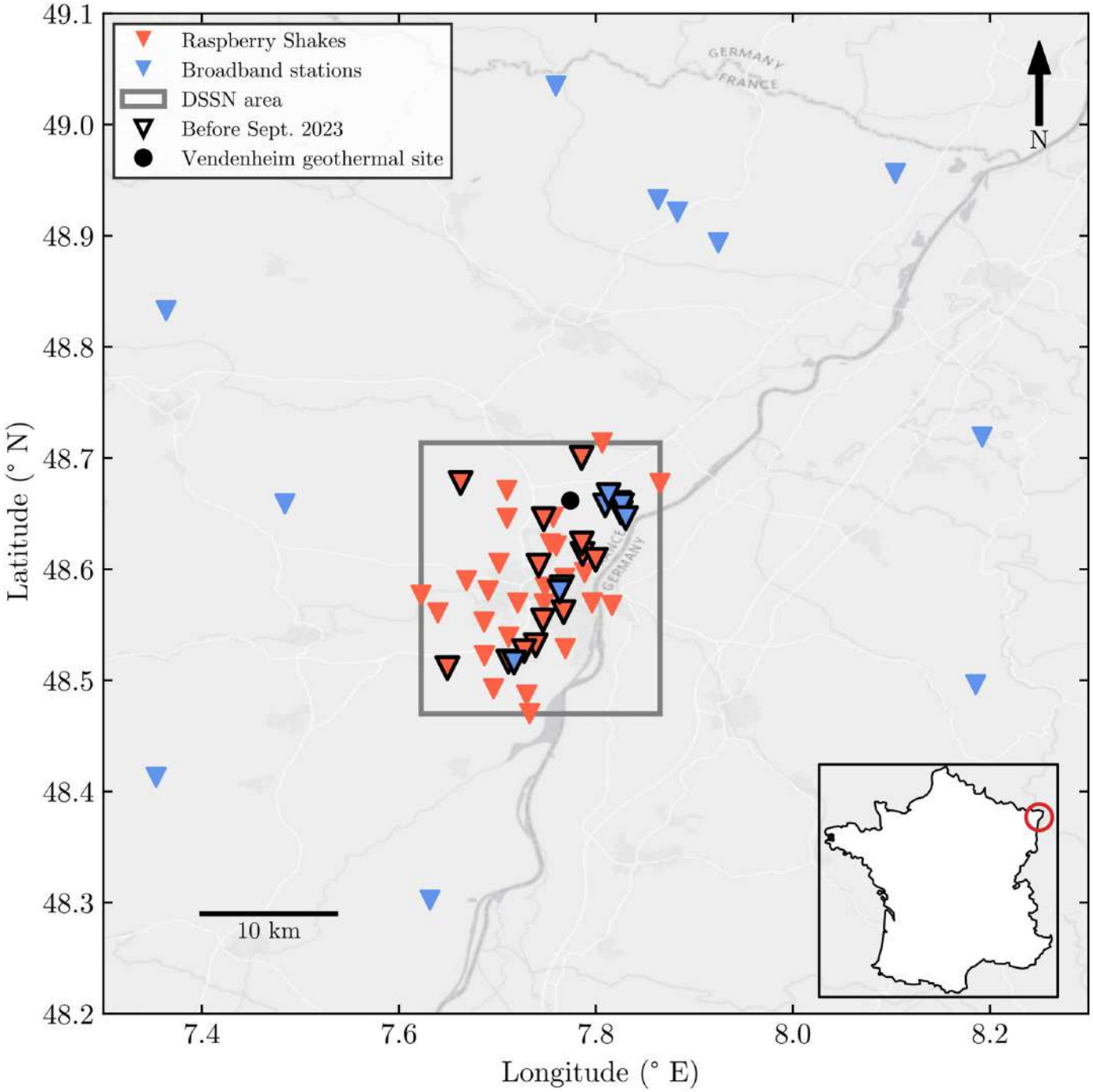

Figure 1. Location of the stations used in the study. The red inverted triangles represent the Raspberry Shake stations, whereas the blue inverted triangles represent the traditional (broadband or short-period) stations. The gray rectangle marks the area covered by the stations part of the Strasbourg dense semipermanent seismic network (DSSN). The DSSN stations with a thicker outline are stations active during the Vendenheim sequence and serve as the reference network throughout the study. The inset shows the location of the study area within France (red circle). The color version of this figure is available only in the electronic edition.

the complete formulation of $\bar{S}$ and to Figure S3 for a visual representation of this method.

Knowing the location of the earthquake sources, it is possible to calculate the WSR for each of the available stations and for different earthquake sizes. The M_c at a given location is then the smallest magnitude needed to reach a predefined WSR threshold at a given number of stations. The following sections explain in detail the methodology we used to derive P_N, P_S, WSR, and M_c for our case study.

Estimation of the noise power (P_N). For each station, we first estimated the noise PPSD of all available components at

each hour of the day to precisely evaluate how noise levels change over the 24 hr of the day and, in turn, to what degree M_c can change at different times of the day. To compute PPSD, we used all available recordings between January 2018 and December 2024.

For each PPSD obtained, we then calculated the modal value of each frequency bin to derive the most probable noise PSD for a given hour and a given component. The hourly PSDs at each station are then averaged across the components. Finally, P_N at a given hour is obtained by integrating the corresponding PSD between 5 and 30 Hz for stations with a sampling frequency of 100 or 200 Hz and between 5 and 23 Hz for stations with a sampling frequency of 50 Hz.

Estimation of the signal power (P_S). We calculated the theoretical earthquake PSDs assuming that the modeled waves are *P* waves. This was done to better facilitate the comparison and validation of our theoretical spectra with the events recorded at the Vendenheim geothermal site because 70% of the picks of the DSSN stations used in the BCSF-Rénass catalog are for *P* waves.

When computing the theoretical PSD, we assumed a stress drop of 4 MPa, a rock density of 2900 kg/m^3, a source–receiver average *P*-wave velocity of 3800 m/s, and an *S*-wave velocity at the source of 3450 m/s. The stress drop corresponds to the average stress drop calculated for the largest events in the catalog, whereas the wave velocities are taken from a 1D velocity model derived from a 3D model inferred at the location of the Geoven wells (Lengliné *et al.*, 2023). We note that the low velocities reflect the thick sedimentary cover at the Vendenheim site, which averages about 3.5 km in thickness (Freymark *et al.*, 2020).

Another parameter required to calculate a theoretical PSD is the quality factor (Q). We estimated this parameter for each station by finding the Q value that minimizes the difference between the theoretical spectra and the observed *P*-wave spectra, averaged over the available components, of the Vendenheim earthquakes. This operation was performed only on earthquakes with a signal-to-noise ratio (SNR) greater than 3 to ensure that the inversion was performed only using waveforms with a limited noise component, leaving 304 of the 582 available events. The Q for a given station was then determined as the average of the Q values calculated for at least 20 events (a condition met by 18 stations in total). Figure S4 shows that using these values, the ratio between the observed and theoretical WSR is, on average, equal to 1, with the observed WSR typically varying within a factor of 2.5 of the theoretical WSR. For stations with fewer than 20 events, we set Q to 230, corresponding to the average Q of stations for which this value could be determined, which ranges from 150 to 300. Finally, we calculated the signal power P_S (equation 3) from the theoretical earthquake PSD using the same integration intervals employed to estimate P_N.

Estimation of the WSR threshold and M_c. We placed the theoretical earthquake sources on a grid with a spacing of 0.1 km and located within the area covered by the DSSN. The grid is positioned at a depth of 4.3 km, corresponding to the average depth of the Vendenheim events in the BCSF-Rénass catalog, which are located between 3 and 6 km depth.

For a given station, the M_c at a grid point is the minimum magnitude required to reach a WSR of 6. We choose this threshold because it corresponds to the WSR value above which the majority (>90%) of the earthquake waveforms recorded by the DSSN stations have a *P*-wave pick in the BCSF-Rénass catalog (Fig. S5). When evaluating the detection capabilities of the network, M_c at a given point is the fourth-lowest M_c at that location. In other words, an event must be recorded by at least four stations. This criterion reflects the fact that in real earthquake catalogs, detections from multiple stations are typically used to confirm an event. In particular, the four-station threshold corresponds to the limit used in the creation of the BCSF-Rénass catalog.

Network configurations

The selection of the WSR threshold and the minimum number of stations required to declare an event can significantly change the estimate of M_c. To avoid reliance on absolute values, our analysis focuses on M_c differences between different station configurations. We considered four configurations: (1) the full DSSN, consisting of 49 active stations; (2) the 11 permanent stations surrounding the DSSN; (3) the early version of the DSSN, with the 22 stations active before the last deployment phase (September 2023); and (4) the combined network of (2) and (3). Figure 1 shows the spatial distribution of these networks.

Using network (3) as the reference, we calculated differences in M_c with respect to the other configurations to analyze how increasing the number of stations, either within or outside the urban area, affects M_c. When comparing the different network configurations, we assumed that all selected stations were active simultaneously. This assumption is made to maximize the number of stations included in the analysis and therefore allow for a more precise evaluation of the impact of the station number on the DSSN performance. Although this may not always reflect reality, it is a reasonable approximation because there are periods when most of the stations in each network configuration are active at the same time (Fig. S6).

Analysis of the relationship between station number and M_c

Taking advantage of the large number of DSSN stations, we also examined how decreasing the minimum interstation distance (and consequently increasing the number of stations) affects M_c within the network. For a given interstation distance ranging from 100 m to 22 km, we built a graph consisting of all stations with at least one station within this distance. For each clique in the graph (i.e., the largest group of stations for which

all interstation distances are equal to or greater than the specified value), we calculated the average M_c within the DSSN. Finally, we averaged the values of M_c and the number of stations for all cliques to determine the M_c and the station count associated with the current minimum distance between stations.

Estimation of location uncertainties maps

Another way to evaluate the performance of a network is to analyze the uncertainties in the earthquake location. Similar to the approach used for the M_c maps, we placed earthquake sources on a grid with a 0.5 km spacing, a depth of 4.3 km, and covering the DSSN area. We set the magnitude of these events to 1.5. This value allows us to compare the location uncertainties calculated when the number of stations is close to the minimum required for location (four stations, during the day) with those calculated when the number of stations is well above this minimum (during the night).

To locate the earthquakes, we adopted the following procedure. Knowing the locations of the events, we first calculated the theoretical arrival times using a 3D velocity model of the area (Lengliné *et al.*, 2023). To simulate pick uncertainty, we added a random Gaussian error to the *P*- and *S*-wave arrival times, with a standard deviation of 0.02 and 0.05 s, respectively. These uncertainty values represent the modal uncertainties assigned to the manual picks found in the BCSF-Rénass catalog.

For each event, we only selected stations that are able to detect it (i.e., stations that have an M_c greater than or equal to 1.5 at the hypocenter location). If a station is able to detect an event, we assumed that both *P* and *S* waves can be picked. The inclusion of both *P* and *S* waves ensures that location uncertainties depend solely on station distribution rather than missing phases, allowing us to better interpret spatial variations.

We then located the events detected by at least four stations with NonLinLoc (Lomax *et al.*, 2000) using the same 3D velocity model used to define wave arrivals. After the location process, we took the square root of the diagonal elements of the covariance matrix to derive the uncertainty in the three directions.

To verify whether the decrease in location uncertainty with an increasing number of DSSN stations follows the same trend as that observed for the magnitude of completeness, we performed the uncertainty estimation process using the reference and full DSSNs.

Analysis of the relationship between station number and location uncertainties. Following the same approach used for M_c, we examined how decreasing the minimum interstation distance (and therefore increasing the number of stations used to locate an event) affects the location uncertainties within the DSSN. The earthquakes are then located using all available stations in a given iteration. In other words, we suppose that the earthquakes have a magnitude large enough to be detected by all stations, thereby eliminating the influence of magnitude and noise conditions on the number of stations available for event location. This approach allowed us to evaluate M_c at greater minimum interstation distances and with a lower number of stations. To reduce computational time, we used for each minimum interstation distance a maximum of 1000 random cliques.

Results

Intra- and interstation noise-level variations

At a given station, P_N levels can vary by up to two orders of magnitude over 24 hr (Fig. 2a), with the noisiest hour being 08:00–09:00 and the least noisy hour being 03:00–04:00 local time. The least noisy hour is defined as the hour with the lowest P_N at most of the DSSN stations. Similarly, the noisiest hour is defined as the hour with the highest P_N at most of the DSSN stations (Fig. S7). We note that the PSD of the recorded noise always remains above the instrument self-noise in the frequency band of interest, even during the quieter hours (Fig. S8).

For a given hour, P_N can vary by more than one order of magnitude between stations (Fig. 2a). Such changes in noise level can also be observed between stations that are less than 1 km apart (Fig. S9). We point out that the broadband stations part of the DSSN, which are hosted in public institutions' buildings or by private entities' buildings, have noise levels comparable to those of the Raspberry Shake stations, which are hosted in private homes (Fig. 2a).

However, at the stations outside the DSSN, noise levels can be several orders of magnitude lower than those observed at the DSSN stations. In addition, the change in noise level between day and night is often limited to less than one order of magnitude (Fig. 2a).

Impact of the noise-level variations on M_c

Significant variations in noise levels between hours of the day and stations lead to similar fluctuations in M_c. Figure 2b shows that for a given DSSN station, the average M_c within the DSSN can often vary by more than 0.5 magnitude units (roughly a threefold change in maximum signal amplitude) over a 24 hr period, and some stations experience differences that exceed one magnitude unit. In contrast, at distant stations outside the DSSN, these variations are generally below 0.5 magnitude units (Fig. 2b).

These fluctuations are also reflected in the network M_c. When using the reference network (i.e., DSSN stations installed before January 2023, Fig. 1), the average M_c within the DSSN increases by approximately 0.7 magnitude units from the least noisy to the noisiest hour (Fig. 3). However, when using the network of distant stations, the average M_c remains more stable throughout the day, varying less than 0.4 magnitude units (Fig. 3).

The difference observed during the least noisy and noisiest hours can be generalized to the time intervals 20:00–08:00 and

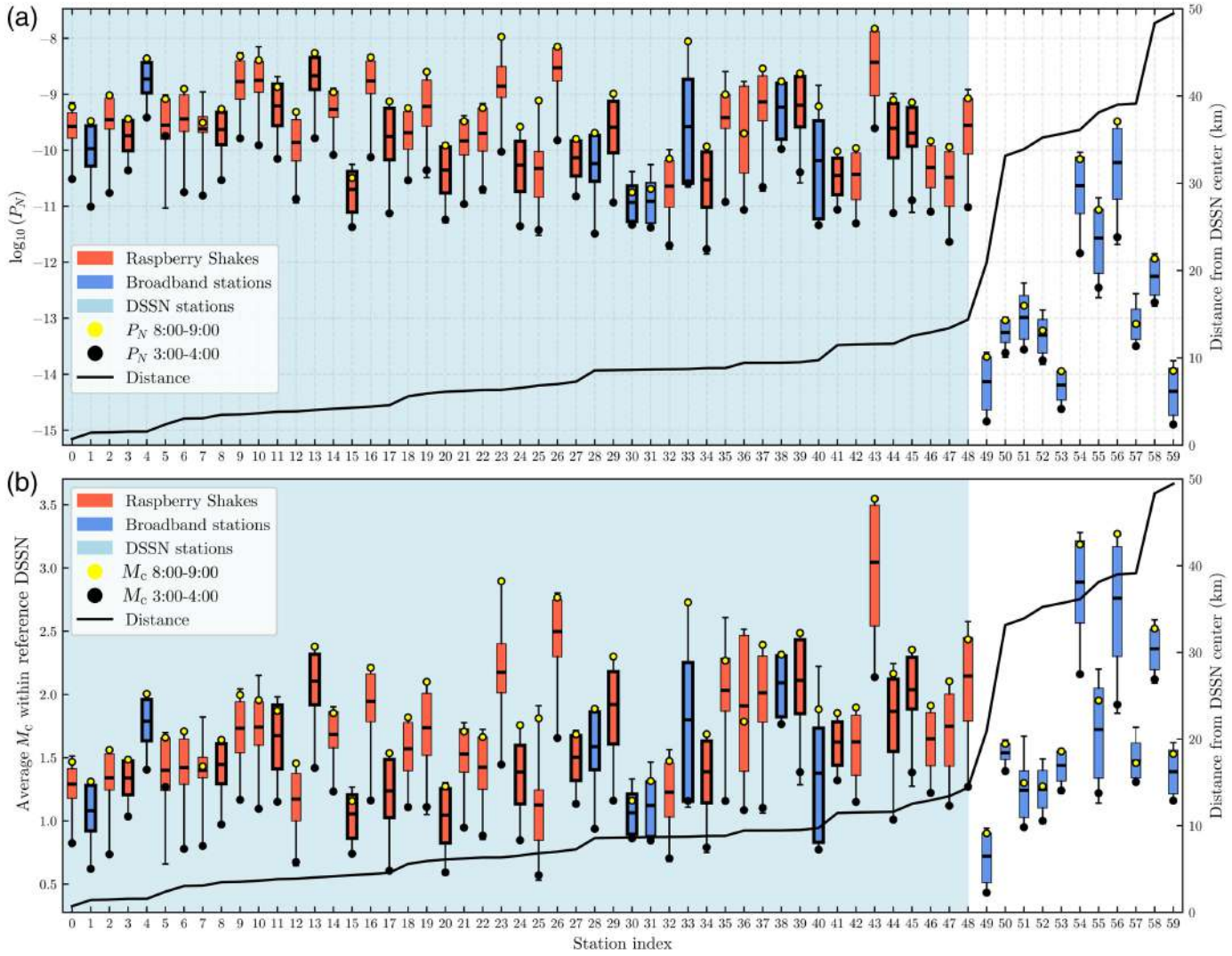

Figure 2. Diurnal variation of noise power (P_N) and magnitude of completeness (M_c) at different stations. (a) Box plot showing the variation of P_N at each station during the 24 hr. The boxes indicate the interval between the first and third quartiles, whereas the whiskers extend from the minimum to the maximum value of P_N. The black tick in the box indicates the average $\log_{10} P_N$ value. The stations are ordered by distance from the center of the DSSN, with the black line indicating their exact distance. The light-blue area highlights the DSSN stations. Boxes with a thicker outline are part of the reference DSSN. (b) Same as panel (a) but using the average M_c within the reference DSSN area instead of $\log_{10}(P_N)$. The color version of this figure is available only in the electronic edition.

08:00–20:00, respectively, because the average M_c in the area remains relatively stable within these periods for the different networks (Fig. 3). Because of the low number of events (582) in the BCSF-Rénass catalog, it is not possible to confirm whether these diurnal variations in M_c can be detected only from observed earthquakes. However, the trend is evident when using a more complete catalog (see Data and Resources; Fig. S10).

Given the large fluctuations in noise levels throughout the day and the generally higher noise levels within the DSSN, particularly during daytime, some DSSN stations are outperformed by, or perform similarly to, stations located more than 30 km away (Fig. 2b). This comparable performance between distant and DSSN stations is also evident in the BCSF-Rénass catalog because three of the five stations with the largest number of *P*-wave picks are outside of the DSSN (Fig. S11).

The difference in M_c between DSSN and the network of distant stations further highlights this trend. During the least noisy hour, the reference DSSN reduces the M_c achieved by the network of distant stations across most of the network's coverage area by up to 0.5 magnitude units (Fig. 4a). However, during the noisiest hour, this improvement is more limited (up to 0.2 magnitude units) and largely restricted to regions with the highest station density (Fig. 4b). In areas with a sparse station coverage, the distant station network achieves M_c values comparable to or even lower than those of the DSSN.

Combining the two networks does not lead to significant improvement during the least noisy hour (Fig. 4c). However, during the noisiest hour and in areas with low station density, it reduces M_c by up to 0.5 magnitude units compared to using

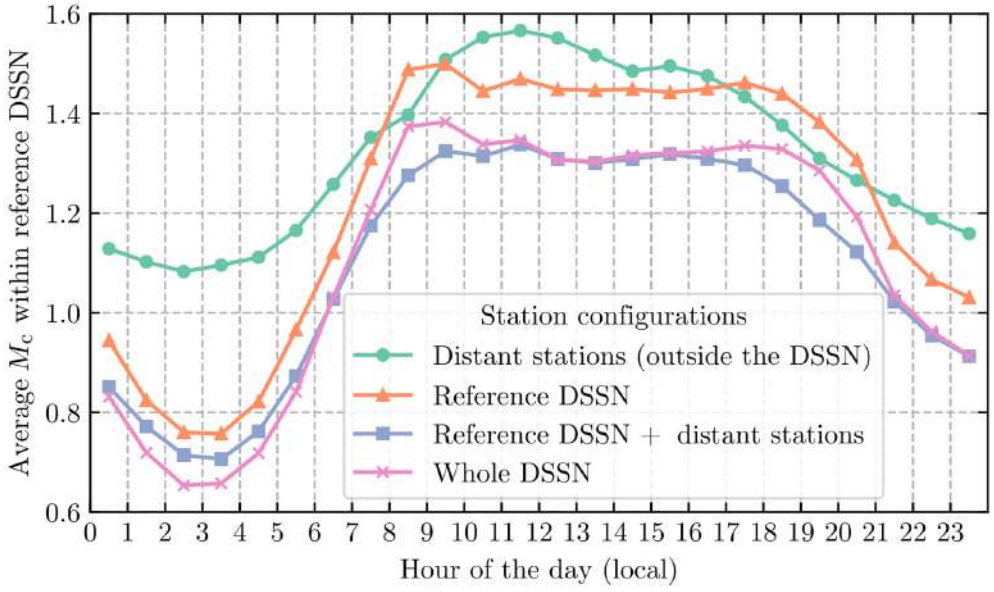

Figure 3. Diurnal variation of M_c, computed as the average of the M_c values estimated within the area covered by the reference DSSN (rectangle in Fig. 4), for different station configurations. The station configurations are defined in the Methods section. Each colored line represents a different configuration. The color version of this figure is available only in the electronic edition.

only the DSSN (Fig. 4d). As a result, the diurnal variation of the average M_c is significantly reduced (Fig. 3).

Impact of network density on M_c. Another way to potentially lower M_c is to increase the number of stations within the region of interest because it can reduce the distance between stations and hypocenters. In 2024, 27 stations, affected by noise levels comparable to those previously installed (Fig. 2), were added to the reference DSSN, thus greatly improving the coverage of the network (Fig. 1); however, the addition of new stations brings modest (<0.2) improvements in M_c within the area both at night and during the day (Fig. 3). Figure 4e,f shows that the reduction in M_c is limited to small areas of low station density, with a decrease of approximately 0.2 magnitude units.

To study at what point increasing the number of stations begins to bring reduced benefits in decreasing M_c, we analyzed how the average M_c within the DSSN varies with both the number of stations n_{stat} and the minimum distance between stations d_{min} (Fig. 5). The relationship between d_{min} and n_{stat} can be empirically approximated by a power law (Fig. 5c) between 2 and 8 km (or between 5 and 30 stations). d_{min} decays as $n_{stat}^{-0.77}$, which lies between the n_{stat}^{-1} behavior expected for d_{min} in a uniformly random distribution of stations and the $n_{stat}^{-0.5}$ behavior expected for the nearest-neighbor model (Clark and Evans, 1954). Below 2 km and above 8 km, the power-law relationship breaks down due to the finite pool of available stations and the imposed minimum network size of four stations, respectively.

Within the range of values in which d_{min} and n_{stat} follow a power law, the change of M_c with d_{min} (Fig. 5a) and n_{stat} (Fig. 5b) can also be approximated by a power law. However, this relationship breaks down at about 3.5 km or 15 stations, before the one that links d_{min} and n_{stat}. This is because, while decreasing d_{min} reduces the average epicentral distance (corresponding in our study to the average distance between the epicenters of the theoretical earthquakes and the station with the fourth-lowest M_c at that position), at short-epicentral distances a given reduction in this value will produce a comparatively small change in the hypocentral distance and therefore in M_c (Fig. 5d). This effect becomes more pronounced with increasing hypocentral depth.

Figure 5 also helps to quantify the significant contribution of distant stations to lowering the average M_c within the DSSN. For example, during the least noisy hour, 4 DSSN stations (d_{min} = 10 km) combined with distant stations reach detection levels comparable to up to 15 DSSN stations (d_{min} = 3.5 km). During the noisiest hour, the DSSN never reaches the M_c levels of the combined network, not even when all available stations are used (n_{stat} = 49 and d_{min} = 0.2 km).

We note that, to derive the relationship between d_{min}, n_{stat}, and M_c, we assumed that all stations are active simultaneously. In practice, even if no new stations are removed or added from the network, stations are not active at all times. The number of available stations is therefore lower and fluctuates over time. For example, the DSSN stations have an average uptime of about 85% (Fig. S6). Assuming conservatively that all stations share the same uptime and that station downtimes are independent, a binomial model predicts that maintaining at least 15 active stations with probability ≥95% would require 21 stations, corresponding to a 40% increase.

Impact of network density on earthquake location uncertainty. We tested whether the addition of new DSSN stations can still improve seismic monitoring, such as by reducing location uncertainty, particularly in depth, even for values beyond which improvements in M_c become limited (d_{min} < 3.5 km or n_{stat} > 15).

Figure 6 shows the change in depth uncertainty within the DSSN for M_L 1.5 earthquakes after the addition of 27 DSSN stations. During the least noisy hour, events within the network are detected and located by the majority of the available

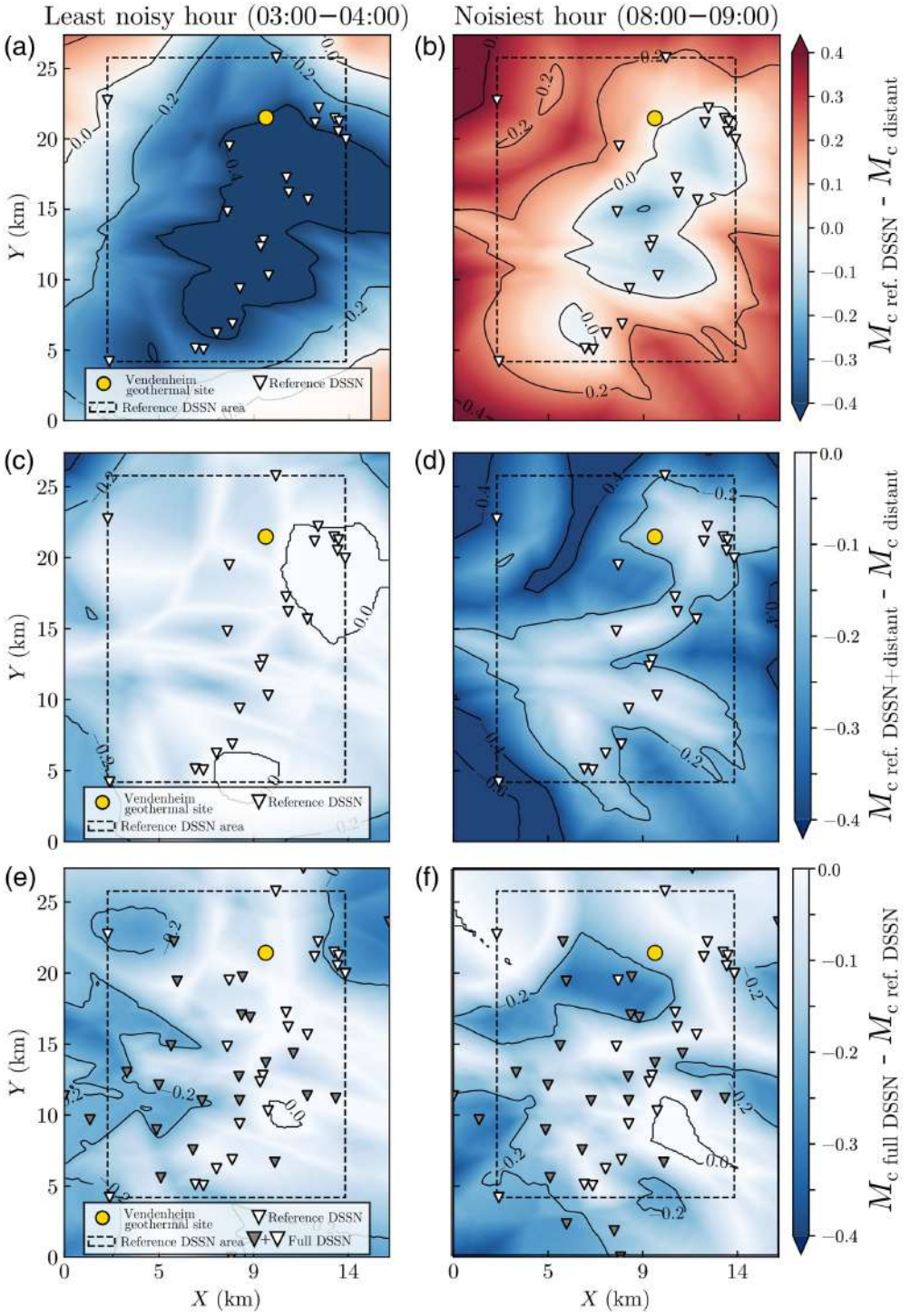

Figure 4. Maps showing the difference between the M_c calculated using different network configurations and at different times of the day. (a,b) Between reference DSSN and distant stations. (c, d) Between the reference DSSN with and without the inclusion of the distant stations. (e, f) Between the full and reference DSSN. The inverted-white triangles represent the DSSN stations, the yellow circle marks the location of the Vendenheim site, and the black rectangle outlines the area covered by the reference DSSN. Coordinates are given in a local Cartesian reference system. The color version of this figure is available only in the electronic edition.

stations (Fig. S13a). In these conditions, uncertainty decreases primarily in low-coverage areas (up to 0.6 km), but also to a lesser extent (by up to 0.2 km) in well-covered areas (Fig. 6a) where no improvement in M_c was observed (Fig. 4e). This improvement is possible because, unlike M_c, location uncertainty continues to decrease as long as the power-law relationship between d_{min} and n_{stat} holds (Figs. 7 and 5c). We point out that if the relationship between d_{min} and n_{stat} remained valid at lower interstation distances, other limiting factors, such as pick uncertainty, would eventually limit further improvements in location uncertainty.

The increase in the number of stations is also beneficial in high-noise conditions, that is, when events are located by only a small portion of the available stations (Fig. S13a). In this scenario, the increase in the number of stations leads to a greater reduction in location uncertainty within the area (Fig. 6). This effect is related to the power-law relationship between location uncertainty and n_{stat}, in which adding a given number of stations to a low-density network has a greater impact on reducing uncertainties than adding it to a high-density one (Fig. 7). More generally, noise conditions affect the number of stations that can detect an event. As a result, location uncertainty shows diurnal fluctuations similar to those observed for the average M_c (Fig. S13). Similar considerations between location uncertainty and the number of DSSN stations can be made for horizontal uncertainties (Fig. S13).

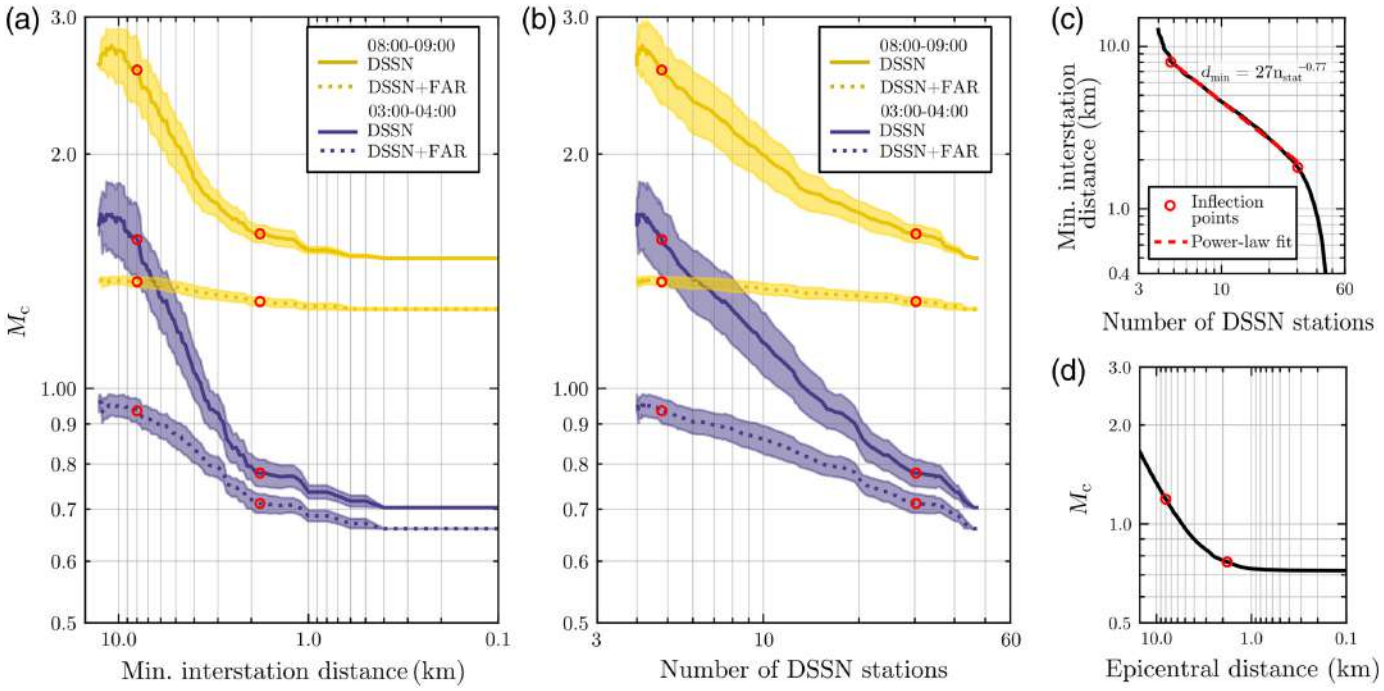

Figure 5. Influence of the number of stations (n_{stat}) and minimum interstation distance (d_{min}) on M_c. (a) Variation of the average M_c within the DSSN with d_{min}. The solid lines represent values calculated using all available DSSN stations, whereas the dashed lines represent values calculated including the distant stations. The yellow lines correspond to values calculated during the noisiest hour, and the purple lines during the least noisy hour. The red circles indicate the inflection points (i.e., the points of maximum curvature) of the relationship between n_{stat} and n_{min} shown in panel (c). (b) Same as panel (a), but with M_c as a function of n_{stat}. (c) Relationship between n_{stat} and d_{min}. (d) Example of how the M_c of one of the DSSN stations varies with epicentral distance. The color version of this figure is available only in the electronic edition.

Finally, we point out that, unlike M_c, the addition of distant stations located in low-noise environments has little influence on lowering depth uncertainty at night and during the day (Fig. S14). However, these stations may still be helpful to reduce horizontal uncertainties in cases for which only a few stations are capable of detecting the events (i.e., during the noisiest hours, Fig. S14).

Discussion and Conclusions

We have evaluated the performance of the Strasbourg DSSN in detecting and locating earthquakes within its coverage area in different noise conditions and by varying the number of active stations.

Anthropogenic noise severely affects the recordings of the DSSN stations, where power noise levels are orders of magnitude higher than those found at some of the permanent stations located in less populated areas and are better protected from noise sources. In addition, noise levels at the DSSN stations vary drastically between night (low-noise conditions) and day (high-noise conditions). As a result, the average M_c within the network can vary by up to 0.6 units between day and night. The timing of these variations (03:00–04:00 and the highest peak at 08:00–09:00) is consistent with those found in other urban areas around the world (e.g., Kheirbek *et al.*, 2014; Batterman *et al.*, 2021).

Under such conditions, the use of permanent stations located at greater distances from the area of interest (between 30 and 40 km in our study), but less affected by anthropogenic noise, can help mitigate the loss of detectability experienced by the local network during the day. In particular, complementing the existing network with these quieter, more distant stations may be more effective in reducing M_c than adding an equal number of stations locally. This is especially true at short d_{min}, in which M_c approaches the minimum-achievable value, which is controlled by hypocentral depth. In this regime ($d_{min} < 3.5$ km or $n_{stat} > 15$ for the analyzed network), the reduction in M_c, which would otherwise approximately follow a power-law decay with decreasing d_{min}, consistent with empirical observations (Mignan *et al.*, 2011), becomes progressively less effective.

However, even when increasing the number of local stations has a limited impact on M_c, it can still improve the determination of seismological parameters and therefore seismic monitoring. For example, we have shown that for earthquakes of a given magnitude, location uncertainty can continue to decrease with shorter interstation distances ($d_{min} < 2$ km or $n_{stat} > 30$) than those observed for M_c. Because the DSSN stations lie within approximately 15 km of the epicenters, the direct *P*- and *S*-wave arrivals recorded by the distant stations (with epicentral distances between 30 and 40 km) carry comparatively

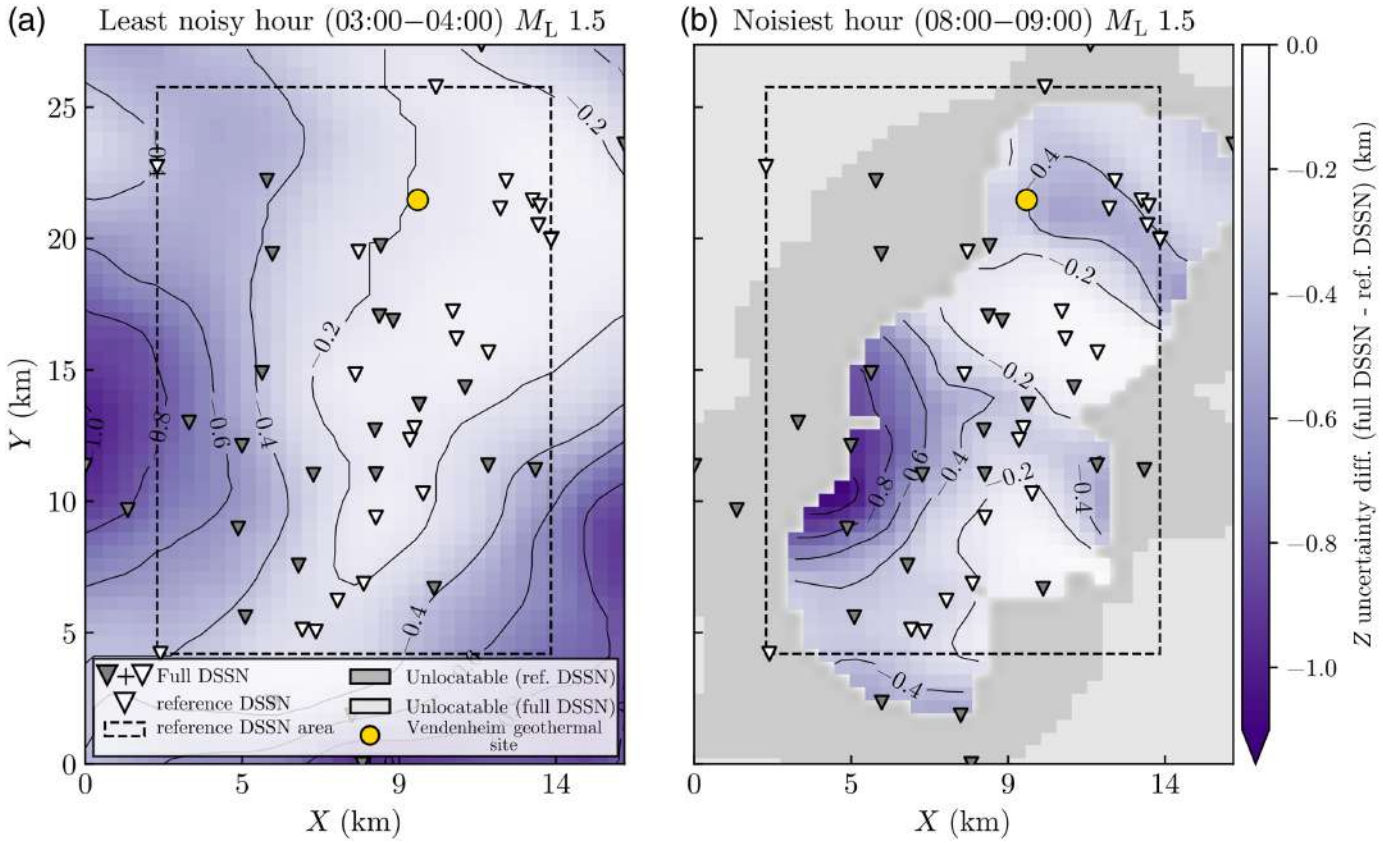

Figure 6. Maps showing the difference between the vertical location uncertainty estimated using full and reference DSSN, assuming at each grid point earthquakes of magnitude 1.5. (a) Uncertainty differences calculated using noise levels from the least noisy hour. (b) Uncertainty differences calculated using noise levels from the noisiest hour. The inverted triangles represent the DSSN stations and the yellow point marks the Vendenheim site, whereas the black rectangle outlines the area covered by the reference DSSN. Regions where conditions needed for locating the earthquake are not met are represented in gray for the reference DSSN and in light gray for the full DSSN. Coordinates are given in a local Cartesian reference system. The absolute vertical uncertainty values for the two station configurations are shown in Figure S12. The average diurnal change is instead shown in Figure S13. The color version of this figure is available only in the electronic edition.

limited depth information for shallow earthquakes. Consequently, although such distant stations can help lower M_c, in such contexts, it is not possible to rely solely on them to build high-resolution catalogs. This highlights the importance of dense urban networks for monitoring induced seismicity in urban areas.

Finally, we note that we estimated location uncertainties in the ideal case in which both *P*- and *S*-wave arrivals can be picked at a station. Under this assumption, single-component (vertical) and three-component stations contribute equally to location uncertainty. In reality, however, at short-epicentral distances, *S*-wave amplitudes are larger on the horizontal components than on the vertical. As a result, *S* waves are more difficult to pick at stations recording only the vertical component. The contribution of these stations to improving location accuracy is therefore reduced.

The findings on M_c and location uncertainty show the importance of evaluating both noise levels, network geometry, and target depth when designing or expanding a seismic network. Failure to do so could lead to either having a large network to maintain with little added benefit in characterizing seismicity, compared to a much smaller network or to a small network in which performance could be significantly improved with few additional stations. In the specific case of the Strasbourg DSSN, we find that adding more than about 30 stations (or reducing the interstation distance below approximately 2 km) offers limited benefit in lowering M_c and location uncertainty for local earthquakes located at 4.3 km depth. Therefore, there are around 20 DSSN stations that contribute little to improving network performance. In practice, these stations still add value by providing redundancy and helping to maintain coverage in case stations are removed or are temporarily unavailable. This is especially relevant for Raspberry Shake stations, which generally have lower uptime than broadband stations (85% vs. 98% on average, respectively; see Fig. S6).

We have also shown that noise levels can vary significantly between stations, regardless of their location or station type. This variation is likely influenced by the differing levels of human activity between neighborhoods, buildings, and residences. Because Raspberry Shake stations are installed in private

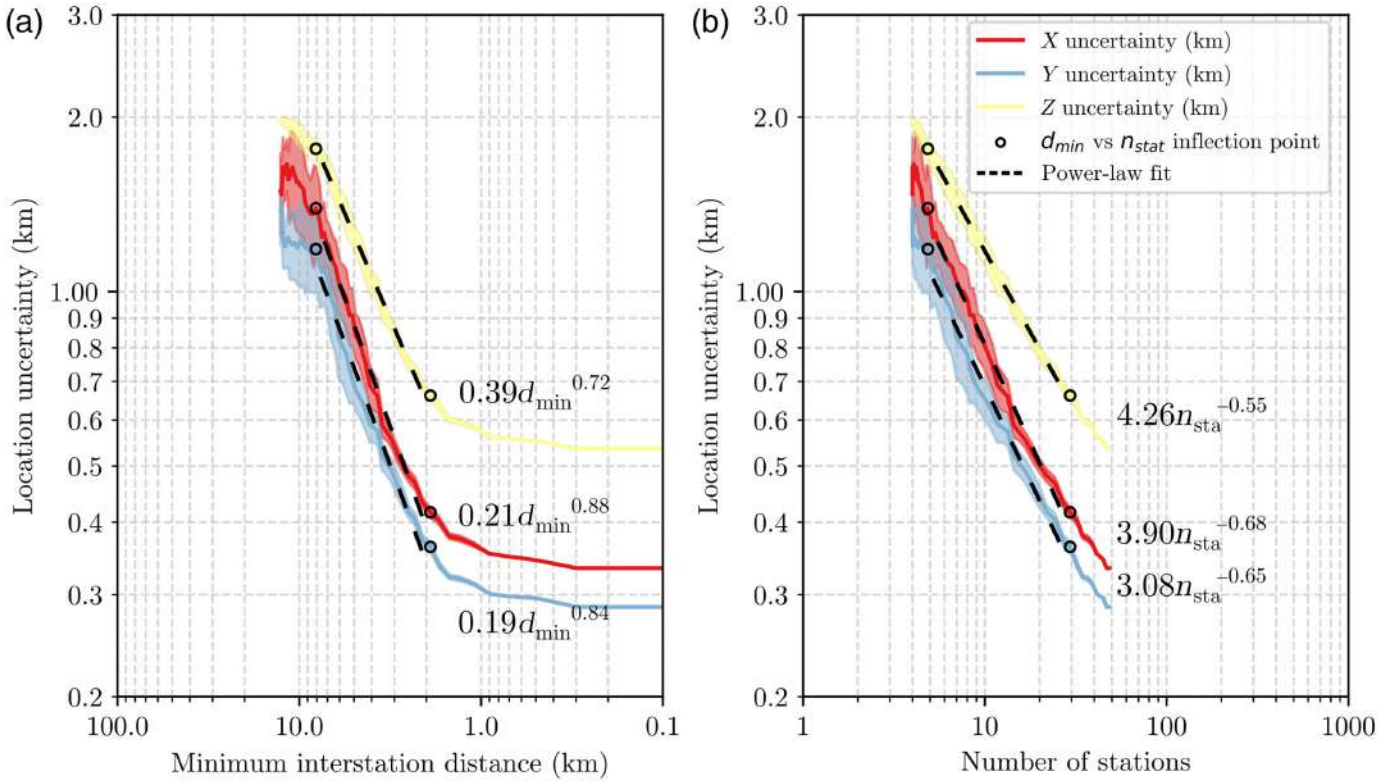

Figure 7. Influence of the number of stations (n_{stat}) and minimum interstation distance (d_{min}) on location uncertainty. (a) Variation of the average location uncertainty within the DSSN as a function of d_{min}, calculated assuming that each event can be detected and thus located by all available stations. (b) Same as panel (a), but as a function of n_{stat}. Each line corresponds to a different direction. Black circles are the points of maximum curvature in the relation between d_{min} and n_{stat} shown in Figure 5c. The color version of this figure is available only in the electronic edition.

homes, our results thus indicate that residential environments do not necessarily exhibit higher noise levels than those found in public or commercial buildings, where DSSN broadband stations are installed. The large variation in noise conditions across stations implies that some sites are significantly better suited for earthquake detection than others. This highlights the critical role of site selection, either through direct noise measurements or noise prediction (e.g., Alam *et al.*, 2017; Keil *et al.*, 2023), in lowering M_c and reducing the impact of noise variability within an urban network, especially in cases where installing a large number of stations is not feasible or practical. If, on the other hand, Raspberry Shake stations can be deployed as a seismic array, with instruments located within the same building or in nearby buildings, the SNR of recorded earthquakes may be improved through stacking techniques (Schweitzer *et al.*, 2012; Fiori *et al.*, 2023). However, their effectiveness should be assessed on a case-by-case basis because it depends on their spatial sampling and the structural characteristics of the buildings. Another option to reduce anthropogenic noise is to install Raspberry Shake stations in shallow boreholes. In urban areas, however, suitable locations can be difficult to find, and this approach substantially increases installation costs, both for site preparation and for the additional equipment required for outdoor deployment. It also reduces maintainability and data accessibility because the instruments are less accessible, and continuous data streaming may not be feasible.

In conclusion, our study indicates that surface seismic stations installed in urban areas, including Raspberry Shake stations, can contribute to more complete and higher-resolution earthquake catalogs and thus can help improve the analysis of natural and induced seismicity. However, achieving reliable detection levels requires either a high station density or a careful selection of high-quality sites. If neither option is feasible, nor if noise levels are excessively high, stations less affected by anthropogenic noise, such as borehole stations or stations located outside urban areas, become essential to compensate for the reduced performance of the urban network.

Data and Resources

In this study, we used waveform data from seismic networks with the International Federation of Digital Seismograph Networks (FDSN) codes AM (Raspberry Shake, 2016), FR (EPOS-France, 1962), and LE (Erdbebendienst Südwest and Rheinland-Pfalz, 2009). Continuous waveforms from the temporary network XX and network 1K have not yet been released to the public. The Bureau Central Sismologique Français and Réseau National de Surveillance Sismique (BCSF-Rénass) catalog of the Vendenheim sequence can be downloaded from https://renass.unistra.fr (last accessed December 2025). The high-resolution

seismicity catalog of the Vendenheim sequence is available on the Data Center for Deep Geothermal Energy (CDGP) platform at https://cdgp.u-strasbg.fr/geonetwork/srv/fre/catalog.search#/metadata/VDHD-Catalogue-Minetto (last accessed November 2025; EOST and Fonroche Géothermie, 2020). The supplemental material provides details on the deployment of the Strasbourg dense semipermanent seismic network (DSSN), the model used to estimate theoretical earthquake spectra, and figures that complement the results presented in this study.

Declaration of Competing Interests

The authors acknowledge that there are no conflicts of interest recorded.

Acknowledgments

The authors thank Hélène Jund and Maxime Bès de Berc for providing the self-noise data of the Raspberry Shake stations, and Pierre Schmittbuhl for useful discussions about network properties. This research was funded in part by the Agence Nationale de la Recherche (ANR) under the PrESENCE Project ANR-21-CE05-0033 and the Clean Energy Transition Partnership (CETP) Geotwins project ANR-24-CETP-0010-01. It was also part of the Geothermica Innovation for de-risking enhanced geothermal energy (DEEP) project. This work of the Interdisciplinary Thematic Institut Geosciences for the energy system transition, as part of the ITI 2021-2028 program of the University of Strasbourg, Centre National de la Recherche Scientifique (CNRS), and Inserm, was supported by Idex Unistra (ANR-10-IDEX-0002) and by the SFRI-STRAT'US Project (ANR-20-SFRI-0012).

References

Alam, M. S., L. Corcoran, E. A. King, A. McNabola, and F. Pilla (2017). Modelling of intra-urban variability of prevailing ambient noise at different temporal resolution, *Noise Mapp.* **4,** no. 1, 20–44.

Anthony, R. E., A. T. Ringler, D. C. Wilson, and E. Wolin (2018). Do low-cost seismographs perform well enough for your network? An overview of laboratory tests and field observations of the OSOP Raspberry Shake 4D, *Seismol. Res. Lett.* **90,** no. 1, 219–228.

Batterman, S., S. C. Warner, T. Xia, S. Sagovac, B. Roberts, B. Vial, and C. Godwin (2021). A community noise survey in Southwest Detroit and the value of supplemental metrics for truck noise, *Environ. Res.* **197,** 111,064.

Bethmann, F., N. Deichmann, and P. M. Mai (2012). Seismic wave attenuation from borehole and surface records in the top 2.5 km beneath the city of Basel, Switzerland, *Geophys. J. Int.* **190,** no. 2, 1257–1270.

Brune, J. N. (1970). Tectonic stress and the spectra of seismic shear waves from earthquakes, *J. Geophys. Res.* **75,** no. 26, 4997–5009.

Calais, E., D. Boisson, S. Symithe, R. Momplaisir, C. Prépetit, S. Ulysse, G. P. Etienne, F. Courboulex, A. Deschamps, and T. Monfret (2019). Can a Raspberry Shake Seismic Network Complement a National Seismic Network? A Case Study in Haiti, *Eos* **100,** doi: 10.1029/2019EO123345.

Çelebi, M. (2019). Highlights of a cursory study of behavior of three instrumented buildings during the Mw 7.1 Anchorage, Alaska, earthquake of 30 November 2018, *Seismol. Res. Lett.* **91,** no. 1, 56–65.

Clark, P. J., and F. C. Evans (1954). Distance to nearest neighbor as a measure of spatial relationships in populations, *Ecology* **35,** no. 4, 445–453.

Clayton, R. W., T. Heaton, M. Kohler, M. Chandy, R. Guy, and J. Bunn (2015). Community seismic network: A dense array to sense earthquake strong motion, *Seismol. Res. Lett.* **86,** no. 5, 1354–1363.

Clayton, R. W., M. Kohler, R. Guy, J. Bunn, T. Heaton, and M. Chandy (2019). CSN-LAUSD network: A dense accelerometer network in Los Angeles schools, *Seismol. Res. Lett.* **91,** no. 2A, 622–630.

Costanzo, A., S. Falcone, A. D'Alessandro, G. Vitale, S. Giovinazzi, M. Morici, A. Dall'Asta, and M. F. Buongiorno (2021). A technological system for post-earthquake damage scenarios based on the monitoring by means of an urban seismic network, *Sensors* **21,** no. 23, 7887.

Diaz, J., M. Schimmel, M. Ruiz, and R. Carbonell (2020). Seismometers within cities: A tool to connect earth sciences and society, *Front. Earth Sci.* **8,** no. 9, doi: 10.3389/feart.2020.00009.

EOST and Fonroche Géothermie (2020). Episode: Geoven geothermal project at Vendenheim, EOST-CDGP.

EPOS-France (1962). EPOS-France broad-band network (RLBP), doi: 10.15778/RESIF.FR.

Erdbebendienst Südwest and Rheinland-Pfalz (2009). Erdbebendienst südwest, doi: 10.7914/SN/LE (in German).

Fiori, R., J. Vergne, J. Schmittbuhl, and D. Zigone (2023). Monitoring induced microseismicity in an urban context using very small seismic arrays: The case study of the Vendenheim EGS project, *Geophysics* **88,** no. 5, WB71–WB87.

Frankel, A., and A. Grant (2020). Site response, basin amplification, and earthquake stress drops in the Portland, Oregon area, *Bull. Seismol. Soc. Am.* **111,** no. 2, 671–685.

Freymark, J., J. Bott, M. Scheck-Wenderoth, K. Bär, M. Stiller, J.-G. Fritsche, M. Kracht, and M. L. Gomez Dacal (2020). 3D-URG: 3D gravity constrained structural model of the Upper Rhine Graben, *GFZ Data Services*, doi: 10.5880/GFZ.4.5.2020.004.

Henao Casas, J. D., and G. Monsalve (2018). Geological inferences about the upper crustal configuration of the Medellin – Aburra Valley (Colombia) using strong motion seismic records. *Geodes. Geodynam.* **9**, no. 1, 67–76.

Herrmann, M., T. Kraft, T. Tormann, L. Scarabello, and S. Wiemer (2019). A consistent high-resolution catalog of induced seismicity in Basel based on matched filter detection and tailored post-processing, *J. Geophys. Res.* **124,** no. 8, 8449–8477.

Hillers, G., T. A. T. Vuorinen, M. R. Uski, J. T. Kortström, P. B. Mäntyniemi, T. Tiira, P. E. Malin, and T. Saarno (2020). The 2018 geothermal reservoir stimulation in Espoo/Helsinki, Southern Finland: Seismic network anatomy and data features, *Seismol. Res. Lett.* **91,** no. 2A, 770–786.

Holmgren, J. M., and M. J. Werner (2021). Raspberry Shake instruments provide initial ground-motion assessment of the induced seismicity at the United Downs Deep Geothermal Power Project in Cornwall, United Kingdom, *Seism. Record* **1,** no. 1, 27–34.

Horne, R., A. Genter, M. McClure, W. Ellsworth, J. Norbeck, and E. Schill (2025). Enhanced geothermal systems for clean firm energy generation, *Nature Rev. Clean Tech.* **1,** no. 2, 148–160.

Hughes, B., F. Illsley-Kemp, E. Mestel, J. Townend, C. Chandrakumar, and R. Prasanna (2025). Using citizen science Raspberry Shake seismometers to enhance earthquake location and characterization: A case study from Wellington, New Zealand, *Seismica* **4,** no. 1, doi: 10.26443/seismica.v4i1.1430.

Janusz, P., P. Bergamo, L. F. Bonilla, F. Panzera, D. Roten, K. Loviknes, and D. Fäh (2024). Multistep procedure for estimating non-linear soil response in low seismicity areas—A case study of Lucerne, Switzerland, *Geophys. J. Int.* **239,** no. 2, 1133–1154.

Keil, S., J. Wassermann, T. Megies, and T. Kraft (2023). Optimal network design for microseismic monitoring in urban areas - A case study in Munich, Germany, *Seismica* **2,** no. 2, doi: 10.26443/seismica.v2i2.1030.

Kheirbek, I., K. Ito, R. Neitzel, J. Kim, S. Johnson, Z. Ross, H. Eisl, and T. Matte (2014). Spatial variation in environmental noise and air pollution in New York City, *J. Urban Health: Bull. New York Acad. Medicine* **91,** no. 3, 415–431.

Küperkoch, L., K. Olbert, and T. Meier (2018). Long-term monitoring of induced seismicity at the Insheim Geothermal Site, Germany, *Bull. Seismol. Soc. Am.* **108,** no. 6, 3668–3683.

Layadi, K., F. Semmane, and A. K. Yelles-Chaouche (2016). Site-effects investigation in the City of Chlef (Formerly El-Asnam), Algeria, using earthquake and ambient vibration data, *Bull. Seismol. Soc. Am.* **106,** no. 5, 2185–2196.

Lecocq, T., S. P. Hicks, K. Van Noten, K. van Wijk, P. Koelemeijer, R. S. M. De Plaen, F. Massin, G. Hillers, R. E. Anthony, M.-T. Apoloner, *et al.* (2020). Global quieting of high-frequency seismic noise due to COVID-19 pandemic lockdown measures, *Science* **369,** no. 6509, 1338–1343.

Lengliné, O., J. Schmittbuhl, K. Drif, S. Lambotte, M. Grunberg, J. Kinscher, C. Sira, A. Schlupp, M. Schaming, H. Jund, *et al.* (2023). The largest induced earthquakes during the Geoven deep geothermal project, Strasbourg, 2018–2022: From source parameters to intensity maps, *Geophys. J. Int.* **234,** no. 3, 2445–2457.

Li, Z., Z. Peng, D. Hollis, L. Zhu, and J. McClellan (2018). High-resolution seismic event detection using local similarity for Large-N arrays, *Sci. Rept.* **8,** no. 1, 1646.

Lomax, A., J. Virieux, P. Volant, and C. Berge-Thierry (2000). Probabilistic earthquake location in 3D and layered models, in *Advances in Seismic Event Location*, C. H. Thurber and N. Rabinowitz (Editors), Springer Netherlands, Dordrecht, The Netherlands, 101–134.

Lythgoe, K., A. Loasby, D. Hidayat, and S. Wei (2021). Seismic event detection in urban Singapore using a nodal array and frequency domain array detector: Earthquakes, blasts and thunderquakes, *Geophys. J. Int.* **226,** no. 3, 1542–1557.

McNamara, D. E., and R. P. Buland (2004). Ambient noise levels in the continental United States, *Bull. Seismol. Soc. Am.* **94,** no. 4, 1517–1527.

Mignan, A., M. J. Werner, S. Wiemer, C.-C. Chen, and Y.-M. Wu (2011). Bayesian estimation of the spatially varying completeness magnitude of earthquake catalogs, *Bull. Seismol. Soc. Am.* **101,** no. 3, 1371–1385.

Miura, H., M. Matsuoka, J. C. Reyes, N. Pulido, M. Hashimoto, A. C. Riaño, A. Hurtado, R. Rincon, H. García, and C. Lozano (2023). Quick estimation model for mapping earthquake impacts in Bogotá, Colombia, *ISPRS Int. J. Geo-Inform.* **12,** no. 12, 471.

Moein, M. J. A., C. Langenbruch, R. Schultz, F. Grigoli, W. L. Ellsworth, R. Wang, A. P. Rinaldi, and S. Shapiro (2023). The physical mechanisms of induced earthquakes, *Nature Rev. Earth Environ.* **4,** no. 12, 847–863.

Pacheco, D., E. D. Mercerat, F. Courboulex, L. F. Bonilla, A. Laurendeau, and A. Alvarado (2022). Profiling the Quito basin (Ecuador) using seismic ambient noise, *Geophys. J. Int.* **228,** no. 2, 1419–1437.

Patanè, D., G. Tusa, W. Yang, A. Astuti, A. Colino, A. Costanza, G. D'Anna, S. Di Prima, G. Fertitta, S. Mangiagli, *et al.* (2022). The Urban Seismic Observatory of Catania (Italy): A real-time seismic monitoring at urban scale, *Remote Sens.* **14,** no. 11, 2583.

Raspberry Shake (2016). Raspberry shake, doi: 10.7914/SN/AM.

Schlupp, A., M. Grunberg, H. Jund, M. Bes-de Berc, M. Turlure, J. Schmittbuhl, O. Lengliné, and J. Vergne (2023). Apport des réseaux sismologiques "SismoCitoyen" déployés en milieu urbain dans l'Hexagone et à Mayotte, in *Actes du 11ème Colloque National de l'AFPS*, Vols. 7–10, Association Française du Génie Parasismique, Guadeloupe, France, 74–79 (in French).

Schmittbuhl, J., S. Lambotte, O. Lengliné, M. Grunberg, H. Jund, J. Vergne, F. Cornet, C. Doubre, and F. Masson (2021). Induced and triggered seismicity below the city of Strasbourg, France from November 2019 to January 2021, *Comptes Rendus. Géosci.* **353,** no. S1, 561–584.

Schorlemmer, D., and J. Woessner (2008). Probability of detecting an earthquake, *Bull. Seismol. Soc. Am.* **98,** no. 5, 2103–2117.

Schultz, R., V. Stern, Y. J. Gu, and D. Eaton (2015). Detection threshold and location resolution of the Alberta Geological Survey earthquake catalogue, *Seismol. Res. Lett.* **86,** no. 2A, 385–397.

Schweitzer, J., J. Fyen, S. Mykkeltveit, S. J. Gibbons, M. Pirli, D. Kühn, and T. Kværna (2012). Seismic arrays, in *New Manual of Seismological Observatory Practice 2 (NMSOP-2)*, P. Bormann (Editor), Deutsches GeoForschungsZentrum GFZ, Potsdam, Germany, 1–80.

Scudero, S., A. Costanzo, and A. D'Alessandro (2023). Urban seismic networks: A worldwide review, *Appl. Sci.* **13,** no. 24, 13,165.

Subedi, S., G. Hetényi, P. Denton, and A. Sauron (2020). Seismology at school in Nepal: A program for educational and citizen seismology through a low-cost seismic network, *Front. Earth Sci.* **8,** doi: 10.3389/feart.2020.00073.

Vasterling, M., U. Wegler, J. Becker, A. Brüstle, and M. Bischoff (2017). Real-time envelope cross-correlation detector: Application to induced seismicity in the Insheim and Landau deep geothermal reservoirs, *J. Seismol.* **21,** no. 1, 193–208.

Vitale, G., A. D'Alessandro, A. Di Benedetto, A. Figlioli, A. Costanzo, S. Speciale, Q. Piattoni, and L. Cipriani (2022). Urban seismic network based on MEMS sensors: The experience of the seismic observatory in Camerino (Marche, Italy), *Sensors* **22,** no. 12, 4335.

Zhou, W., F. Lanza, I. Grigoratos, R. Schultz, J. Cousse, E. Trutnevyte, A. Muntendam-Bos, and S. Wiemer (2024). Managing induced seismicity risks from enhanced geothermal systems: A good practice guideline, *Rev. Geophys.* **62,** no. 4, e2024RG000849, doi: 10.1029/2024RG000849.

Zülfikar, A. C., N. Ö. Z. Fercan, S. Tunç, and M. Erdik (2017). Real-time earthquake shake, damage, and loss mapping for Istanbul metropolitan area, *Earth Planets Space* **69,** no. 1, 9.

Manuscript received 24 July 2025
Published online 31 December 2025